

Detection of X-ray Emission from the Warm-Hot Intergalactic Medium through the Angular Autocorrelation Function with Chandra

M. Galeazzi¹, A. Gupta², K. Hufenberger, and E. Ursino

Physics Department, University of Miami, Coral Gables, FL 33124

ABSTRACT

We have used the angular Autocorrelation Function (AcF) on the angular scale of a few arcminutes to detect and characterize the emission from the Warm-Hot Intergalactic Medium (WHIM) in a pointing with Chandra's ACIS-S instrument. We focused our attention on the energy bands 0.4-0.6 keV, where the WHIM emission is expected to be strongest, due to the redshifted O VII and O VIII lines, and 0.7-0.9 keV, where the WHIM emission is expected to be significantly smaller.

After removing identified point sources, and any spurious signal due to detector background and unidentified point sources, in the lower energy band we found a clear AcF signal that we attribute to the WHIM, with a statistical significance of several sigmas ($\chi^2 = 129$, $N = 31$). The attribution of the signal to the WHIM (and not to other spurious emissions, such as unresolved point sources) is confirmed by the higher energy band where the signal is compatible with zero.

1. Introduction

Understanding the discrepancy between the amount of baryons measured at high and low redshift has been the subject of extensive investigation in recent years both from the theoretical and observational point of view. In particular, the focus of the scientific community has been on the nature of the Warm-Hot Intergalactic Medium (WHIM), a warm, filamentary structure with density 20 to 1000 times the critical density of the universe and temperature greater than 5×10^5 K filling intergalactic space.

¹Corresponding author, galeazzi@physics.miami.edu

²Current address: Department of Astronomy, Ohio State University, Columbus, OH 43210

Although hydrodynamic simulations all agree on the existence of such gas, and predict that about half of the baryons in the current universe are “hidden” in such filaments (Cen & Ostriker 2006; Borgani et al. 2004), detecting and characterizing the WHIM has been difficult. At these temperatures and densities the baryons are in the form of highly ionized plasma, making them essentially invisible to all but low energy X-ray and UV observations, mostly through excitation lines of highly ionized heavy elements. However, the WHIM contribution to the total emission in these bands is weak and is expected to be on the order of 10-15% in the soft X-ray band (Takey et al. 2011; Ursino & Galeazzi 2006; Ursino et al. 2009). Highly ionized metals in the WHIM are also responsible for absorption features whose strength is rather weak (Branchini et al. 2009). The current clearest detection of the WHIM comes from absorption lines in the FUV spectra of bright, distant sources (Danforth et al. 2006; Danforth & Shull 2008; Tripp et al. 2008). However, FUV absorbers trace primarily the warm gas ($T < 10^6$ K) and the bulk of the WHIM is expected to be at higher temperatures, characterized by soft X-ray features whose detection is more difficult. A small number of investigations have successfully detected the WHIM signal through soft X-ray absorption and emission measurements. In particular, absorption features have been identified in the soft X-ray spectra of distant quasars (Nicastro et al. 2005; Buote et al. 2009; Fang et al. 2010), and emission from one filament has been detected (Werner et al. 2008). Our group has also successfully identified the WHIM signal in emission using a statistical approach based on the angular Autocorrelation Function (AcF) of data from XMM-Newton (Galeazzi et al. 2009). The WHIM filaments are expected to have a characteristic angular structure with a typical scale of a few arcminutes, leaving a signature in the angular distribution of their X-ray emission that can be identified on top of other components of the Diffuse X-ray Background (DXB) (Ursino et al. 2011). We have performed a new measurement to detect the WHIM signal using the AcF with Chandra ACIS-S data. The significantly higher angular resolution of Chandra (compared to XMM-Newton) allows us to better remove the signal from point sources and extend our investigation to lower angular scales. To have a significant effective area in our energy band of interest, we used the Back-Illuminated (BI) chip of the ACIS-S instrument, with an effective area of about 100 cm^2 at 0.5 keV. The smaller field of view of the Chandra pointing compared to our previous investigation, however, introduces a bias in the measured AcF that must be removed in order to use the data for further analysis.

In this paper we first introduce our data reduction (section 2) and analysis (section 3) methods, then discuss our AcF result (section 3). We also use a technique we developed to remove the bias from the AcF result to extract a “clean” AcF signal and compare it with our simulation to characterize the WHIM gas responsible for the emission (section 4).

2. Observation and data reduction

To study the AcF properties of the DXB we focused on the Blanco Cosmology Survey (BCS) region due to the large amount of multiwavelength data available for the region. In particular we pointed to a region at coordinates RA=79.25 and DEC=-52 (from now on the Blanco Field) with the lowest Hydrogen column density of the BCS. We used the 100 μm maps from the *Infrared Astronomical Satellite (IRAS)* to evaluate the neutral hydrogen density in the Blanco Field. The *IRAS* average brightness is 2.9 MJy sr⁻¹. Using the typical high-latitude 100 $\mu\text{m}/N_{\text{H}}$ ratio of $0.85 \times 10^{20} \text{ cm}^2 \text{ MJy sr}^{-1}$ (Boulanger & Pérault 1988), the evaluated neutral hydrogen density is $0.5 \times 10^{21} \text{ cm}^{-2}$.

For our analysis, we requested a total of 150 ks of observing time, which were broken into six *CHANDRA* pointings performed with the ACIS-S instrument between November 2010 and January 2011. The aim point was centered on the BI chip (ACIS-S3) to take advantage of the better response at low energy. Around 0.5 keV the BI chip on ACIS-S provides an effective area 5-10 times bigger than the Front Illuminated (FI) ones, which is crucial to study the very faint signal from the DXB. The characteristics of the six pointings are reported in Table 1. The first 2 ks of observation 13129 were characterized by a CCD temperature 5 K higher than the usual operation temperature, but the amplitude and distribution of the pulses were not affected. For observation 13196, an area in the bias area of CCD 2 (ACIS-S2) suffered from anomalous high data values, however we did not use data from CCD 2 since it is one of the FI chips.

For data reduction and point source detection we used tools from the *CXC/CIAO* package¹. Since the six observations have different roll angles (column 4 of Table 1), we aligned all the datasets to match observation 13214 (the one with longest observation time) using the tool *reproject_events*. With *dmextract* and *deflare* (method sigma, nsigma=3) we generated lightcurves and extracted the good time intervals (GTI) for each dataset. We filtered the datasets using the GTIs, energy in the 0.3 – 2 keV, and CCD 7 (ACIS-S3) only. The choice of CCD 7 only is rather straightforward, since it is the chip with highest response at low energies and it corresponds to the aimpoint for ACIS-S. A second filtering with the desired energy interval (i.e. [400 – 600] eV and [700 – 900 eV]) and “bin sky=8” is used to generate maps for the single datasets. Exposure maps corresponding to each individual pointing were also generated using the tools *asphist*, *mkinstmap*, and *mkexpmap*. As the weight spectrum to generate the exposure maps, we used a model with an unabsorbed thermal component (APEC), an absorbed thermal component (APEC), and an absorbed power law. The parameters for the three components are reported in Table 2. The parameters are taken from

¹CIAO 4.3 <http://cxc.harvard.edu/ciao/>

McCammon et al. (2002) and we did not renormalize to the *CHANDRA* field of view, since the normalization is not important for the weights.

In addition to the $[400 - 600]$ eV and $[700 - 900]$ eV maps used for the AcF analysis, we also generated maps in the energy ranges $[0.5 - 2]$ keV, $[2 - 7]$ keV, and $[0.5 - 7]$ keV for detection of point sources. We applied the tool *wavdetect* to the three maps, with 3 iterations and radius scale of “2 – 4” pixels and found 36, 97, and 44 sources with a flux limit of 4.59×10^{-16} ergs s $^{-1}$ cm $^{-2}$, 8.75×10^{-16} ergs s $^{-1}$ cm $^{-2}$, and 6.42×10^{-16} ergs s $^{-1}$ cm $^{-2}$ respectively.

In Fig. 1 we show the $[0.4-0.6]$ keV map obtained by superposing the six *Chandra* observations of the Blanco Field. The green contours represent the point sources identified in the $[2.0-7.0]$ keV band. On the *right* panel we show the corresponding exposure map.

3. Data Analysis

3.1. The Angular Autocorrelation Function

The angular distribution of a signal as a function of the angular separation θ can be characterized by the angular Autocorrelation Function ($w(\theta)$). For X-ray diffuse emission, the estimator is based on the difference in X-ray flux between different areas of an image and takes the following general form (Soltan et al. 1999):

$$w(\theta) = \frac{\langle s(n)s(n') \rangle}{\mu^2} - 1, \quad (1)$$

where $s(n)$ is the signal’s intensity in the direction n , $s(n)s(n')$ is the product of intensities with angular separation θ , and μ is the mean value of the signal.

The AcF is also the tool routinely used to characterize the spatial distribution of point sources, such as Active Galactic Nuclei (AGNs), galaxies, etc. For point sources the estimator is given by the number of pairs DD with angular separation θ divided by the expected number of pairs for a random distribution RR with the same average and sampling geometry (Landy and Szalay 1993):

$$w(\theta) = \frac{DD}{RR} - 1. \quad (2)$$

Different algorithms to implement the AcF for point sources have been derived and Landy and Szalay (1993-*LS* from now on) have compared several of them to evaluate their accuracy and bias under different conditions. As part of their analysis, *LS* introduced a new,

Poisson limited, algorithm:

$$w(\theta) = \frac{DD - 2DR + RR}{RR}, \quad (3)$$

where DR is the expected number of pairs between data and random distribution.

The AcF has also been used for the characterization of photon distributions from diffuse emission, and specifically the WHIM. In our previous work with X-ray maps, we introduced an algorithm to deal with X-ray rate maps (Ursino & Galeazzi 2006; Galeazzi et al. 2009). The algorithm uses the signal count rate (R) of each pixel, weighted by the exposure time (e) of that pixel:

$$w(\theta) = \frac{\sum_{i=1, N_\theta} \sum_{j=i+1, N_\theta} (R_i - \bar{R})(R_j - \bar{R}) \sqrt{e_i e_j}}{\sum_{i=1, N_\theta} \sum_{j=i+1, N_\theta} \sqrt{e_i e_j}} \cdot \frac{1}{\bar{R}^2}. \quad (4)$$

where the sum is over the N_θ pairs of pixels separated by θ and \bar{R} denotes the average count rate. Ursino et al. (2011) have also suggested the use of a variation of the LS for diffuse emission, where, instead of the number of pairs, the corresponding fluxes are used. That is, Eq. 3 is used for all pixel pairs in the image and each pair is weighted by the product of the two fluxes. Ursino et al. (2011) have also shown that this method is mathematically identical to Eq. 4.

For completeness, in this work we used three approaches:

1. the algorithm described by Eq. 4;
2. the algorithm introduced by Ursino et al. (2011). i.e., Eq. 3 used over all pixel pairs in the image, with each pair weighted by the product of the two fluxes;
3. the LS algorithm (Eq. 3) assuming that each photon in the image corresponds to a point source. If one pixel contains more than one photon, each photon is considered as a separate source, all with the same coordinates. Considering that in our Chandra image the number of pixels is much bigger than the number of photons (roughly 10/1), this is a very efficient and fast algorithm from the computational point of view.

As expected, our comparison of the three approaches has shown that, in fact, all three approaches produce identical AcFs, and none of our conclusions that follow depend on the method used. The choice between them therefore depends only on the investigator's personal preference.

3.2. Implementing the AcF with Chandra

As discussed before, the Chandra data used for this investigation consist of 6 different pointings, with the same pointing direction, but not necessarily the same rotation around the pointing axis. This required particular care in the analysis of the data, especially for the calculation of the average value (\bar{R}) to use for the AcF calculations. We describe here the steps we took:

- we began with the separate count and exposure maps for each of the six observations, rather than the single merged image;
- we generated a cumulative spectrum for all pointings and used the Chandra standard tools to evaluate the instrumental background spectrum². To generate the background spectrum we used the ACIS stowed background event file relative to ACIS-S3. We modified the header and reprojected the stowed data according to the dataset pointing (*reproject_events*). With *specextract* we extracted the spectra for the DXB and the corresponding particle background in the field of view. For each energy band this step allows us to estimate the background ratio, i.e., the fraction of background events vs. total events;
- we used the previous two steps to generate a distribution map for each pointing. The distribution map contains the expected number of counts for each pixel. It was generated assuming that there are two contributions to the count maps, a flat distribution across the whole area of the CCD with total number of counts equal to the estimated number of background events and a distribution modulated by the exposure map of the pointing with total number of counts equal to the total number of non-background events;
- finally, we added the individual distribution maps and renormalized the sum to obtain a probability map. The probability map was then used to generate the random map in the implementation of the AcF algorithms based on *LS*. It was also used for the implementation of Eq. 4. The equation requires that the map mean be constant and we achieve this either by dividing the counts by the probability maps, or by subtracting the expected background from the counts and dividing by exposure. These produce equivalent results. We note that this approach is essentially equivalent to the one suggested by Cappelluti et al. (2011), where instead of subtracting the total average, a “local” average was used and the AcF was calculated using a map of “residuals”;

²<http://cxc.harvard.edu/ciao/threads/acisbackground/>

- in the process, we also added the individual count maps to obtain the total count map for AcF calculations.

We point out that, in our previous work with XMM-Newton data (Galeazzi et al. 2009) the procedure implemented was simpler due to the fact that we were dealing with a single pointing. In that case, we used the general average over the whole map for the AcF calculation and removed the effect of background afterward by quantifying it. While the procedure used for XMM-Newton data was more than adequate in that instance, the new procedure developed here is more robust and can be used in a much larger variety of situations. We extensively tested its robustness and found that it is sensitive to the value of the background ratio. In particular, the use of an incorrect background ratio (either higher or lower) has the effect of increasing the value of the calculated AcF. However, the procedure is self correcting and can, in fact, be used to calculate the background ratio independent of the energy spectrum. In fact, the bias due to an incorrect background ratio always increases the absolute value of the AcF, whether the background is bigger or smaller. Therefore the correct value of the background ratio can be determined by minimizing the absolute value of the AcF at all angles. We note that, in our data, for both energy ranges considered, the background ratio estimated this way was in perfect agreement with the one obtained through the study of the energy spectrum.

4. Results

4.1. Measuring the AcF in the Blanco Field

Similarly to what we have done in our previous work (Galeazzi et al. 2009), we focused our attention to two separate energy bands, 0.4-0.6 keV and 0.7-0.9 keV. The lower energy band was chosen to maximize the signal from the WHIM, as it is the band where low redshift oxygen lines are expected to have a significant contribution. The higher energy band was chosen as a control band, particularly for removing the effect of point sources, as that band is expected to have a still significant contribution to the AcF from point sources, but very little contribution from the WHIM (Ursino & Galeazzi 2006; Ursino et al. 2010).

In our analysis, we combined all sources found as described in section 2 and removed them from both energy bands. We then followed the procedure described in section 3.2 to generate a count and a probability image for each band. From the analysis of the energy spectra, we used background ratios of 0.85 for the 0.4-0.6 keV band and 0.81 for the 0.7-0.9 keV one. We then used the algorithms described in section 3.1 to compute the angular autocorrelation function for both bands. As in our previous work, we initially set a threshold

on exposure to remove pixels with very low exposure. However, we verified that our procedure is quite immune to the threshold's value and we obtained equivalent results by varying the threshold from 0.1 to 0.5 of the maximum exposure. We only noticed an effect when the threshold was set even higher, but that was due to the fact that, in that case, the solid angle used in the calculations becomes too small and the result is significantly affected by bias, as discussed in section 4.2.

For the calculation of the AcF, we used the angular interval of 7.8 arcsec to 8 arcmin to maximize the region of interest for the WHIM, within the angular size of the BI chip. Finally, to remove the contribution of unresolved point sources we used the same procedure described in Galeazzi et al. (2009). The threshold to identify point sources in the 0.5-2 keV band was 4.59×10^{-16} ergs s⁻¹ cm⁻². The AcF of unresolved point sources was evaluated using the correlation of identified sources. This was then rescaled based on the ratio of fluxes of identified and unresolved sources and removed from the total AcF. The flux of unidentified point sources was quantified using data from McCammon et al. (2002). The comparison of the two energy bands was also used to verify the validity of the procedure. We point out that, in the angular scale of interest for the WHIM, the contribution of residual, unidentified point sources is minimal, and becomes significant at low angular scales (< 1 arcmin).

The result of our analysis is reported in Fig. 2. The figure shows the calculated AcF in the 0.4-0.6 keV (red line) and 0.7-0.9 keV (blue line) energy band. To estimate the statistical significance of our result we generated 1,000 random maps, with zero expected AcF at all angles and the same count distribution of our data, using the probability maps. We then calculated the standard deviation and used it as an estimate for the error in the AcF measurements. The result shows that, in the 0.4-0.6 keV band the AcF signal is different from zero with a significance of several sigmas ($\chi^2 = 129$, $N = 31$). At the same time, the AcF signal in the 0.7-0.9 keV band is compatible with zero ($\chi^2 = 15.6$, $N = 31$), confirming that the contribution of point sources has been properly removed. The black datapoints in Fig. 2 represent the AcF with its standard deviation derived from the 1,000 iterations of random maps with zero AcF. The gray lines represent a subsample of 100 of those iterations.

It is worth pointing out that, in fact, the simple use of the standard deviation is not quite the correct method to estimate the statistical significance of the results, as it does not take into account the fact that each datapoint in our measured AcF is not just different from zero, but it is also correlated with nearby datapoints. To properly test the statistical significance of our results we used the 1,000 simulations to generate a covariance matrix and used such matrix to calculate χ^2 . Using the standard deviation to calculate χ^2 corresponds to using only the diagonal terms in the matrix and, indeed, if we do that we get the same result. However, when we use the full matrix we get a much higher value of $\chi^2 = 2,273$.

This is due to the fact that, indeed, our AcF data have a specific distribution, which is much less likely to be generated just by random fluctuations. We stress that, with either approach, the detection of the AcF signal is indisputable.

Figure 3 shows the AcF data, for the band 0.4-0.6 keV, (black dots), together with the previous XMM-Newton data scaled to Chandra’s FOV (black line). The gray area represents the cosmic variation in the XMM-Newton data (Galeazzi et al. 2009). As is evident from the figure, although the Chandra data are slightly higher than the XMM-Newton average, they are (mostly) well within the expected cosmic variation and statistically in agreement with the XMM-Newton results. The figure also shows the expected AcF signal as predicted by our simulations (Ursino et al. 2011; Takey et al. 2011) scaled assuming that 12% of the total Diffuse X-ray Background is due to the WHIM, as derived from the XMM-Newton data. The simulation is in good agreement with our data above 1 arcmin, although it increases much more rapidly below 1 arcmin.

Figure 4 shows the same AcF data (black line), for the band 0.4-0.6 keV, with logarithmic x-scale. The gray region represent the cosmic variance derived from the measurement. We generated 1,000 fields $2 \text{ deg} \times 2 \text{ deg}$ using a Gaussian distribution with the net total AcF equal to the measured one. From each large field we then extracted a smaller one matching our Chandra exposure map and we calculated its AcF. The standard deviation for the 1,000 AcF obtained was then combined with the statistical error in our measurement to obtain the gray area shown.

Focusing on the black line in the figure, in addition to the non-zero signal already discussed, there are two additional features that are worth noting. The first one is the fact that the signal is positive below 3-4 arcmin and negative above, the second is a distortion in the signal. Both features are due to a bias in the data due to the limited FOV of Chandra’s single chip used. The FOV used is about 8 arcmin, comparable to the angular scale of the WHIM signal. This necessarily implies that, when calculating the AcF, the average used in the calculations is not a true average of the signal, but just a local one, which is biased by the same data used in the calculations.

4.2. AcF Bias

The issue of bias in the AcF calculation due to a limited FOV has already been discussed in details in the literature in the context of point sources (see. for example, Coleman & Pietronero (1992); Landy and Szalay (1993); Bernstein (1994); Kerscher (1999)). In Huppenberger et al. (2012) we report a complete treatment of bias for a diffuse emission and an AcF calculated

using the expression in Eq. 4 in the presence of a background signal. The analysis shows that the bias has two effects, one is the distortion of the AcF signal itself, the other is a constant bias in the AcF. The first effect can be reversed and the distortion removed. However, there is a degeneracy in the AcF value with respect to any constant added to the signal that cannot be removed without making additional assumptions.

In practice the integral of the calculated AcF, over the whole scale of the survey area is zero. This explains why, for our small survey area, the signal is positive for small angular scales and negative for large angular scales. The AcF bias can be estimated with the support of simulations. Specifically, simulations of the WHIM signal (Ursino et al. 2011) indicate that the WHIM AcF goes to zero asymptotically at large angles, above 6-8 arcmin. A reasonable approach is therefore to add a constant to the AcF signal to cancel the AcF average at the largest angles covered by the survey (in our case 6 to 8 arcmin).

Figure 4 shows the AcF data after the corrections due to bias distortion (red line) and bias distortion plus constant value (blue line). As described before, to remove the bias constant we assumed that the AcF is close to zero above 6 arcmin and used the average AcF value from 6 to 8 arcmin to calculate the constant value. We note that the AcF behavior does not follow a power law behavior and is much “flatter” at low angles compared to the behavior derived from WHIM simulations (Ursino et al. 2011).

5. Conclusions

We have detected and characterized the angular distribution of the WHIM using the angular AcF. We have detected an AcF signal attributed to the WHIM with a statistical significance of several sigmas. The result is in agreement with our previous work with XMM-Newton data and, at angular scales above 1 arcmin with our simulations of the WHIM signal, assuming that 12% of the diffuse x-ray background in the energy band 0.4-0.6 keV is due to the WHIM.

We also looked at the shape of the measured angular AcF as a function of the separation angle θ and found that it does not increase at low angular scales as much as expected from simulations.

This work was supported by NASA through the Smithsonian Astrophysical Observatory (SAO), Award #G0112177X.

REFERENCES

- Bernstein, G. M., 1994, *ApJ*, 424, 569.
- Borgani, S. et al., 2004, *MNRAS*, 348, 1078
- Boulanger, F., & Pérouault, M., 1988, *ApJ*, 330, 964
- Branchini, E., et al., 2009, *ApJ*, 697, 328
- Buote, D. A., et al. 2009, *ApJ*, 695, 1351
- Cappelluti, N., et al., talk given at the 2nd Cervia Workshop on WHIM, Cervia, Italy, 6/20-6/21, 2011
- Cen, R., Ostriker, J. P., 2006, *ApJ*, 650, 560
- Coleman, P. H., & Pietronero, L., 1992, *Phys. Rep.*, 213, 311
- Danforth, C. W., et al., 2006, *ApJ*, 640, 716
- Danforth, C.W., & Shull, J.M., 2008, *ApJ*, 679, 194
- Fang T., Buote D. A., Humphrey P. J., Canizares C. R., Zappacosta L., Maiolino R., Tagliaferri G., Gastaldello F., 2010, *ApJ*, 714, 1715
- Galeazzi, M., Gupta, A., & Ursino, E. 2009, *ApJ*, 695, 1127
- Huffenberger, K., Galeazzi, M., & Ursino, E., 2012, submitted to *ApJ*
- Kerscher, M., 1999, *A&A*, 343, 333.
- Landy S. D., Szalay A. S., 1993, *ApJ*, 412, 64 (LS)
- McCammon, D., et al., 2002, *ApJ*, 576, 188
- Nicastro, F., et al., 2005, *Nature*, 433, 495
- Takei, et al., 2011, *ApJ*, 734, 91
- Tripp, T. M., Sembach, K. R., Bowen, D. V., Savage, B. D., Jenkins, E. B., Lehner, N., & Richter, P., 2008, *ApJS*, 177, 39
- Soltan, A. M., et al., 1999, *A&A*, 349, 354
- Ursino, E., & Galeazzi, M., 2006, *ApJ*, 652, 1085

Ursino, E., Branchini, E., Galeazzi, M., Marulli, F., Moscardini, L., Piro, L., Roncarelli, M., & Takei, Y., 2009, MNRAS, 414, 2970

Ursino, E., Galeazzi, M., & Roncarelli, M., 2010, ApJ, 721, 46.

Ursino, E., Branchini, E., Galeazzi, M., Marulli, F., Moscardini, L., Piro, L., Roncarelli, M., Takei, Y., 2011, MNRAS, 414, 2970

Werner, N., et al., 2008, A&A, 482, L29.

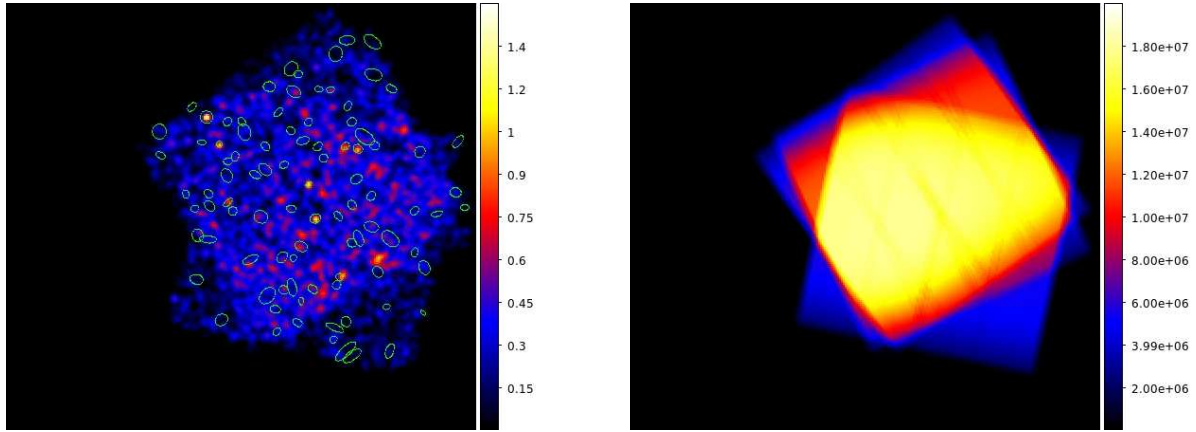


Fig. 1.— (*Left*) *Chandra* map of the Blanco Field in the $[0.4 - 0.6]$ keV energy band. The color bar is in units of counts s^{-1} . (*Right*) Corresponding exposure map, in units of s cm^2 . The images is $15 \text{ arcmin} \times 12 \text{ arcmin}$.

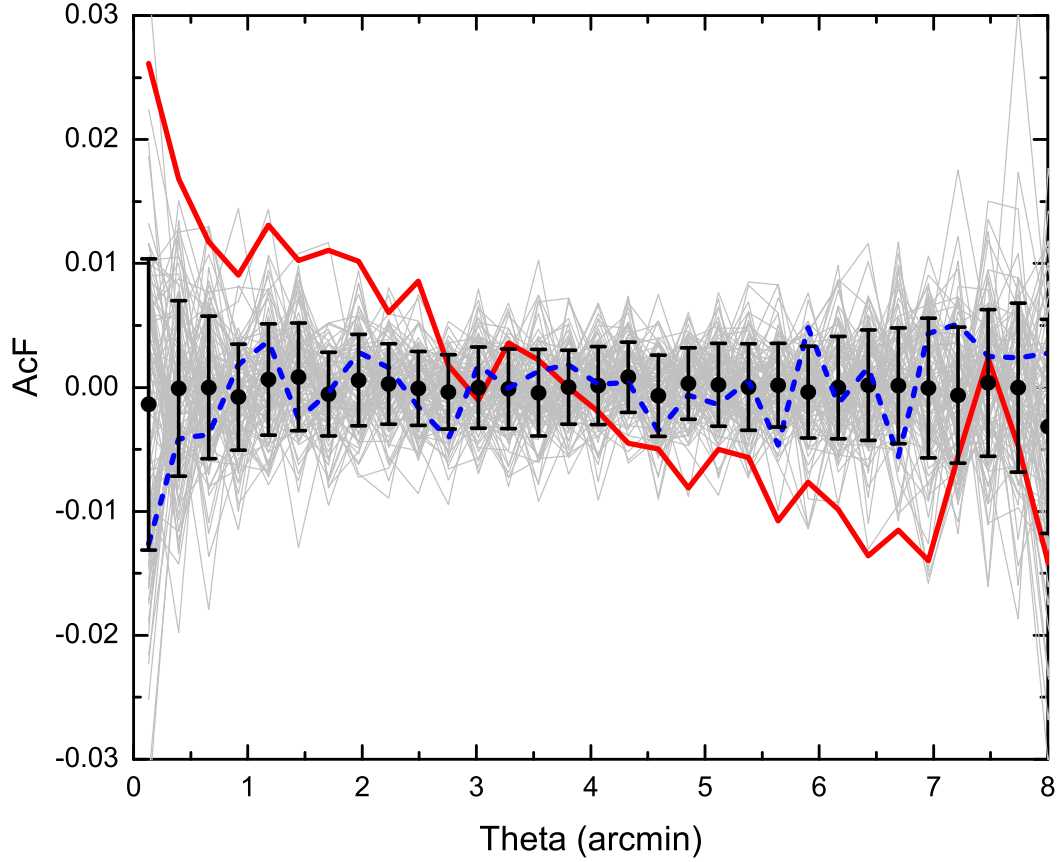


Fig. 2.— Calculated AcF in the energy band 0.4-0.6 keV (red line) and 0.7-0.9 keV (blue line). The black datapoints represent the AcF with its standard deviation derived from 1000 iterations of random maps with zero AcF. The gray lines show 100 of those iterations.

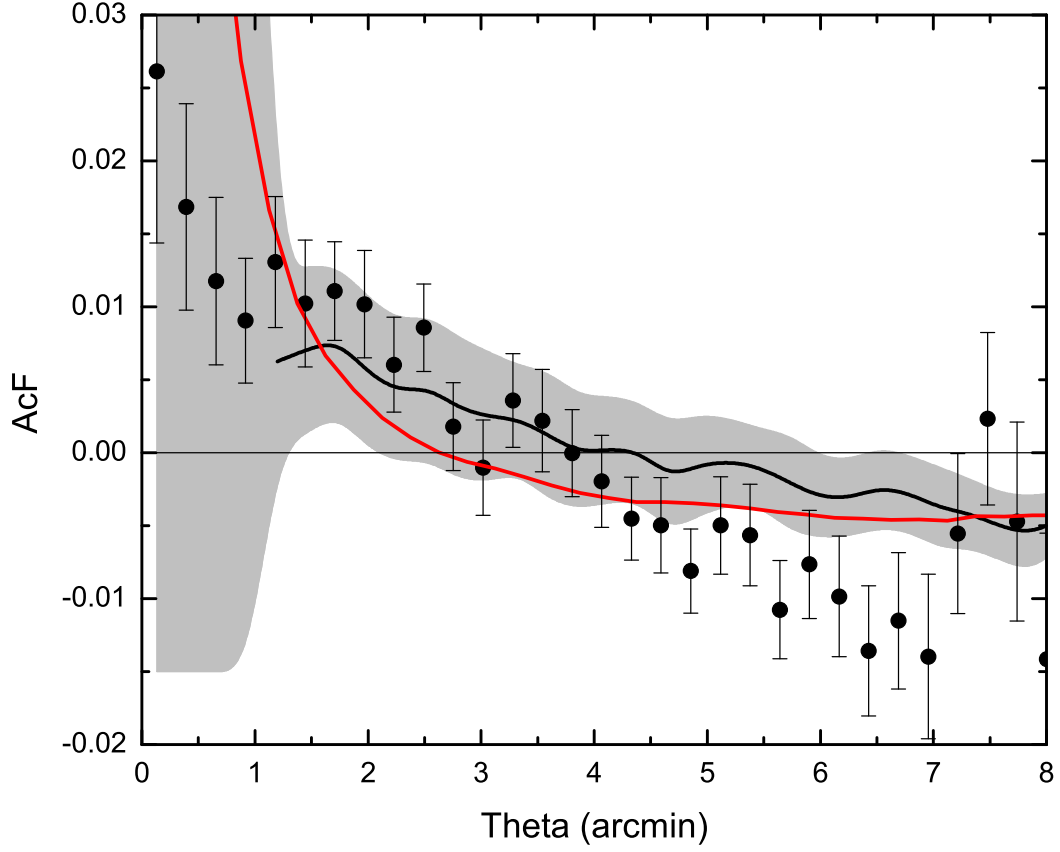


Fig. 3.— AcF data from our Chandra field (black dots), together with the previous XMM-Newton data scaled to our FOV (black line). The gray area represents the cosmic variation in the XMM-Newton data. The red line represents the expected AcF from WHIM simulations, with a constant bias added for the best match to the data.

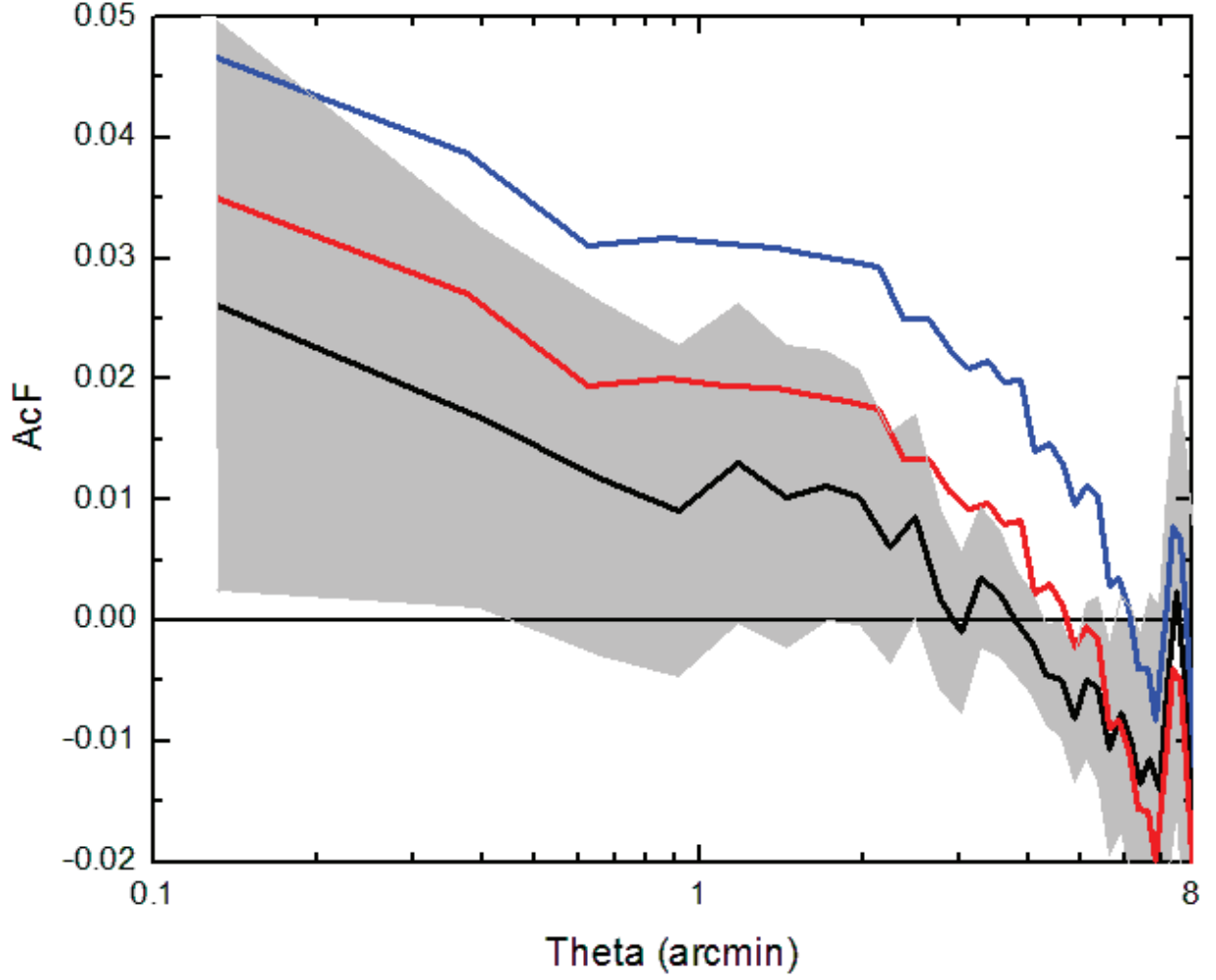


Fig. 4.— Calculated AcF in the energy band 0.4-0.6 keV (same as in Fig. 2) in logarithmic scale (black line). The gray area represents the cosmic variance derived from the data. The red and blue lines represent, respectively, the same AcF signal after only the bias distortion, and the bias distortion and constant value have been removed.

Table 1. Observations of Blanco Field.

ID	RA_nom (deg)	DEC_nom (deg)	roll_nom (deg)	livetime (s)	Observation Date
12924	79.2557	-51.9967	12.1111	19794	30 Nov 2010
13129	79.2579	-52.0004	324.1628	27199	16 Jan 2011
13130	79.2578	-51.9994	335.1628	12391	13 Jan 2011
13196	79.2557	-51.9966	12.1111	27692	13 Dec 2010
13214	79.2578	-51.9994	335.1628	34602	15 Jan 2011
13216	79.2579	-52.0004	324.1628	27200	17 Jan 2011

Table 2. Parameter for spectral weight.

Model	Parameter	Value
Apec 1	KT	0.099 keV
Apec 1	Metallicity	1 Z/Z_{\odot}
Apec 1	redshift	0
Apec 1	Normalization	17.6
Apec 2	KT	0.225 keV
Apec 2	Metallicity	1 Z/Z_{\odot}
Apec 2	redshift	0
Apec 2	Normalization	7.4
Power Law	Photon Index	1.52
Power Law	Normalization	12.3